The Reddest Atmospheric Modes and the Forcings of the Spectra of These Modes

JIN-SONG VON STORCH

Institute of Meteorology, University of Hamburg, Hamburg, Germany

(Manuscript received 3 August 1995, in final form 9 July 1998)

ABSTRACT

The reddest atmospheric modes are studied using a 500-yr integration performed with the coupled ECHAM1/LSG general circulation model. By fitting a first-order autoregressive process to the considered time series, a simple measure of the spectral shape is obtained that allows an objective intercomparison of the spectra and the time series. Two modes, the tropical and the Southern Hemisphere modes, are identified as the reddest modes of the model atmosphere. Both are strongly anisotropic. The Southern Hemisphere mode, characterized by a dipole of zonal wind anomalies at Southern Hemispheric mid- and high latitudes, is related to a mass redistribution and a well-defined meridional circulation, whereas no significant anomalies of surface pressure and meridional velocity are found for the tropical mode, which is characterized by a maximum of zonal wind anomalies in the upper tropical troposphere. On timescales longer than a month, the two modes make, relative to other motions, the largest contributions to the global axial relative and Ω angular momenta M_r and M_Ω (i.e., the portions of the angular momentum that are related to the relative motions and the distributions of mass, respectively) and control the variations of M_r and M_Ω. Based on these relationships, the separated budgets of M_r and M_Ω are used to study the forcings of the spectra of the modes. The results suggest that the forcings of the low-frequency parts of the spectra are extremely feeble, whereas the forcings of the high-frequency parts of the spectra can be easily captured. For the Southern Hemisphere mode, the forcings of the high-frequency variations involve processes that are related to large meridional velocity near the surface.

1. Introduction

In recent years, climate variations on long timescales have drawn more and more attention from researchers. Concerning the atmospheric variability, James and James (1989) considered an integration of about 100 yr obtained with a simplified atmospheric circulation model, with the annual cycle being the only external forcing of the system. They found that the atmospheric flow can be variable on timescales of about 10–40 yr. Several other studies followed, again using long integrations of simplified atmospheric models to describe the spatial structures and to analyze the mechanisms of long-term variations found in these runs (James and James 1992; Yu and Hartmann 1993; Robinson 1991, 1993). The results suggested that the atmosphere can generate variations at timescales longer than the annual cycle.

The results of simple models raise the question of which atmospheric motion has the longest timescale. This is, however, not a simply answered question, since both observed and simulated data suggest that atmospheric time series exhibit variations on a wide range of timescales. In the frequency domain, variances are normally spread out over all frequencies. In terms of the spectrum, the above question may be rephrased as, which motion has a spectrum with the highest spectral energy level at the lowest frequency. Such a spectrum is a red spectrum. This paper considers the question of which atmospheric motion has the reddest spectrum. For this purpose, long time series of various atmospheric variables are needed. Since the available observational data are too short for spectral estimates at frequencies down to one cycle every few decades, the first 500 yr of a 1260-yr integration with the coupled University of Hamburg Climate Model (ECHAM1/LSG) general circulation model (GCM) are considered. A description of the coupled model and the 1260-yr integration is given by von Storch et al. (1997).

Characteristic of the reddest modes in the ECHAM1/LSG integration are their relationships to the atmospheric axial angular momenta. The global absolute atmospheric angular momentum M_a can be split into the relative angular momentum M_r, which is a function of the relative motions, and the Ω angular momentum M_Ω, which is a function of the atmospheric mass distribution. The budget of M_a is the sum of the budgets of M_r and M_Ω. If one is interested in the variations of M_a, as has been the case in many previous angular momentum studies using both observed and simulated data (see, e.g.,

Corresponding author address: Dr. Jin-Song von Storch, Institute of Hydrophysics, GKSS—Research Center, D-21502 Geesthacht, Germany.
E-mail: jinsong.von.storch@gkss.de

Rosen 1993; Boer 1990), there is no need to study the separated budgets of M_r and M_Ω. The focus of this paper, however, is different. It will be shown that one of the reddest modes is related to the variations of M_r and the other to the variations of M_Ω. Due to these relationships, it is obvious that the study of the separated budgets will help in the understanding of the forcings of the reddest modes.

Using the formulation of the relative and Ω axial angular momenta of a unit volume given by Peixoto and Oort (1992), the separated budgets of M_r and M_Ω of a dry atmosphere are obtained by applying the integral over the atmospheric volume. One has

$$\frac{dM_r}{dt} = -\mathcal{C} + \mathcal{F} + \mathcal{P} \tag{1}$$

$$\frac{dM_\Omega}{dt} = \mathcal{C} \tag{2}$$

with

$$M_r = \frac{2\pi r^3}{g}\int_{p_s}^{0}\int_{\pi/2}^{-\pi/2}[u]\cos^2\varphi\, d\varphi\, dp \tag{3}$$

$$M_\Omega = \Omega I_a = \frac{2\pi r^4\Omega}{g}\int_{-\pi/2}^{\pi/2}[p_s]\cos^3\varphi\, d\varphi \tag{4}$$

and

$$\mathcal{C} = \frac{2\pi r^3\Omega}{g}\int_{p_s}^{0}\int_{-\pi/2}^{\pi/2}[v]\sin\varphi\cos^2\varphi\, d\varphi\, dp \tag{5}$$

$$\mathcal{F} = \int_s r\cos\varphi\tau_o\, dS \tag{6}$$

$$\mathcal{P} = -\int_s\left(p_s\frac{\partial z_o}{\partial\theta}\right)dS, \tag{7}$$

where Ω is the angular velocity of the earth, g gravity, r the radius of the earth, φ latitude, u (v) zonal (meridional) velocity, and p_s surface pressure. The surface integral is denoted by $\int_s dS$. A zonally averaged value is indicated by [ ]. The moment of inertia of the atmosphere is I_a.[1] Friction torque $\mathcal{F}$, pressure torque $\mathcal{P}$, and the Coriolis conversion term $\mathcal{C}$ result from global integrations of the friction force, the zonal pressure gradient, and the Coriolis force, respectively. In Eqs. (1) and (2) $\mathcal{C}$ describes the conversion between the relative and the Ω angular momentum. It is assumed in (5) that vertical velocity can be neglected relative to meridional velocity. An equatorward flow will lead to a decrease in its relative angular momentum, equal in magnitude to an increase in its Ω angular momentum. In (6) τ_o is the zonal component of the stress exerted by the underlying medium on the atmosphere. In (7) $\partial z_o/\partial\theta$ represents the zonal gradient of the elevation of the earth's surface. In this paper, the vertical integrals are calculated using values at 1000, 900, 700, 500, 400, 300, 200, 100, and 50 hPa.

Section 2 deals with the identification of the motions that have the reddest spectra. Section 3 describes the spatial characteristics of the identified modes. Section 4 deals with the relationships between the reddest modes and the global axial relative and Ω angular momenta. The forcings of the spectra of the reddest modes are discussed in section 5. A summary is given in the final section.

2. Identification of the reddest modes

This paper assumes that large-scale motions have more low-frequency variance than small-scale motions. Following this assumption, the reddest modes are expected to be modes described by large-scale patterns. Such patterns will be defined as the leading EOFs of the global anomaly fields of various variables obtained from the ECHAM1/LSG integration. The reddest mode may be derived by considering the spectra of the EOF coefficients (or principal components, PCs) and comparing them with each other.

a. A measure of the redness

Many atmospheric variables can be approximated by a first-order auto-regressive [AR(1)] process. Denoting the process parameter by α, which is simply the lag-1 correlation of the considered time series, and the spectrum of the driving noise by Γ_n, the spectrum Γ of the AR(1) process is given by

$$\Gamma(\omega) = \frac{\Gamma_n(\omega)}{1 - 2\alpha\cos(2\pi\omega\Delta) + \alpha^2},$$

where Δ is the time increment of the time series and ω the frequency measured in units of $1/\Delta$. For $\omega \ll 1/(2\pi\Delta)$, the above equation reduces to

$$\Gamma(\omega) = \frac{\Gamma_n(\omega)}{(1-\alpha)^2 + \alpha(2\pi\Delta\omega)^2}.$$

For a white driving noise with $\Gamma_n(\omega) = \text{const.}$, the shape of the spectrum that is described by $\Gamma(\omega)/\Gamma_n(\omega)$ is determined entirely by α. The spectral shape is characterized at the high- and low-frequency limits by

$$\Gamma(\omega)/\Gamma_n(\omega) = \begin{cases} 1/\alpha(2\pi\Delta)^2\omega^2 & \text{for } \omega \gg \omega^* \\ 1/(1-\alpha)^2 & \text{for } \omega \ll \omega^*, \end{cases} \tag{8}$$

with ω^* being defined as follows:

$$\omega^* = \left(\frac{1-\alpha}{2\pi\alpha^{1/2}}\right)\frac{1}{\Delta}.$$

The spectral shape $\Gamma(\omega)/\Gamma_n(\omega)$ increases with de-

[1] In Eq. (4), the offset effect of the deformable earth, which can be described by using an appropriate Love number, is not included.

creasing ω at the rate of $1/\omega^2$ for $\omega \gg \omega^*$ and reaches a constant level at frequencies satisfying $\omega \ll \omega^*$. In a log–log plot, the low- and high-frequency parts of the spectrum can be approximated by two straight lines. The high-frequency one has a ω^{-2} slope and the low-frequency one lies parallel to the frequency axis. The frequency at which the spectrum bends to merge the two lines is given by ω^*. Hereafter, $1/\omega^*$ is also referred to as the bending timescale. A smaller ω^* (i.e., a larger $1/\omega^*$) leads to a wider frequency band over which the spectral energy increases at the rate of ω^{-2} and a higher spectral level at frequency $\omega \ll \omega^*$. Thus, the spectral shape of an AR(1) process is determined by the frequency ω^*. In the following, the bending timescale $T_o = 1/\omega^*$ is used as a measure of the redness of the spectrum shape. Without information about the spectral level of the white noise, no statement can be made about the absolute low-frequency variances.

b. The reddest time series

The time series of the coefficients associated with the leading EOFs of the atmospheric variables are now considered. The analysis is concentrated on the streamfunction and the velocity potential, which completely describe horizontal motions. In order to additionally capture vertically varying motions, the streamfunction and velocity potential at 200, 500, and 850 hPa is considered. The EOFs are calculated from 500-yr monthly unfiltered anomaly fields. Anomalies are obtained by subtracting the 500-yr means of each calendar month.

The bending timescale $T_o = 1/\omega^*$ of the first 10 leading PCs for the streamfunction and velocity potential at the chosen levels is shown in Fig. 1. For velocity potential, the only large value is obtained from the sixth PC at 850 hPa. The corresponding EOF pattern (not shown) shows large anomalies near the Antarctic, indicating that this mode is related to the initial drift of the sea ice during the coupled integration (von Storch et al. 1997). Apart from this value, T_o of the streamfunction (Fig. 1b) is noticeably larger than that of the velocity potential (Fig. 1a). The result suggests that the nondivergent flow is much redder than the nonrotational flow.

The largest T_o values, up to about 11 months, result from the first two PCs of the stream function. The T_o of the higher-order PCs in Fig. 1b is about 2–3 months. The values of the first two PCs, however, vary with altitude. At 850 hPa, T_o of the second PC becomes very small. Consideration of the first two EOF patterns at the different levels indicates that they essentially describe two modes with different vertical structures. The mode described by the first EOF at 200 hPa loses its dominance at 500 and 850 hPa. It will be shown in section 3 that this mode is located in the upper troposphere. For this reason, no large value of T_o can be found at 850 hPa. In contrast to that, the mode described by the second EOF at 200 hPa is barotropic and remains that

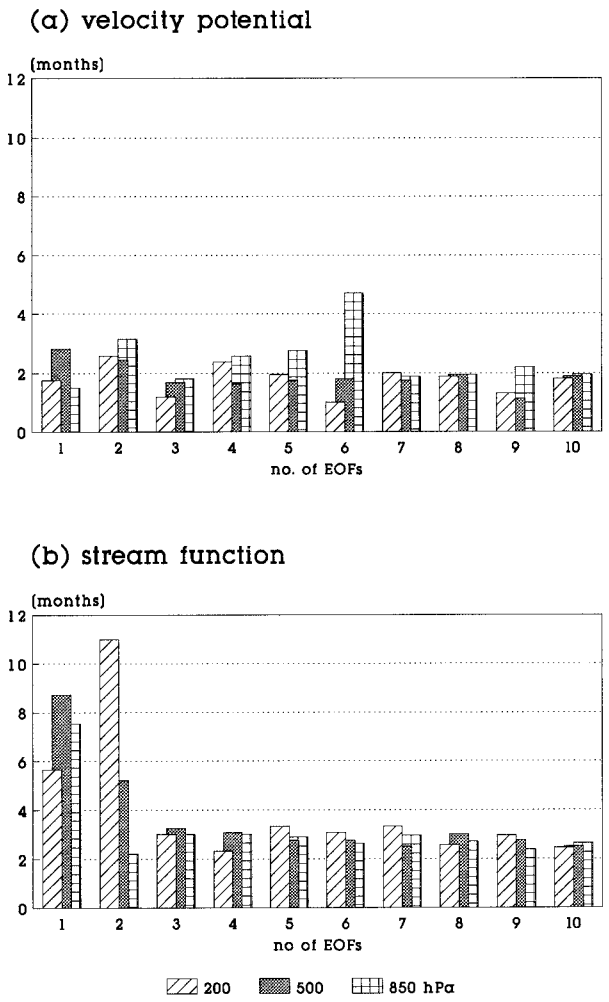

FIG. 1. The bending timescale T_o (in months) as functions of the orders of EOFs. The values of T_o are derived from the PCs of (a) the velocity potential and (b) the streamfunction at 200, 500, and 850 hPa.

strength throughout the troposphere. It becomes the first EOF at 500 and 850 hPa. Roughly speaking, PC2 at 200 hPa and PC1 at 500 and 850 hPa represent one mode, and PC1 at 200 hPa and PC2 at 500 and 850 hPa the other mode. In the following, the modes described by PC1 and PC2 of the 200-hPa streamfunction are considered as the reddest atmospheric modes in the ECHAM1/LSG integration. One should not be confused by the EOF order. The leading EOFs capture the largest portion of the lag-0 covariance, but their coefficient time series need not possess any of the specific temporal characteristics that are described by the covariance functions at nonzero lags.

Consideration of the spectra shows that, relative to the spectra of other PCs, the spectra of the first two PCs of the 200-hPa streamfunction indeed become flat at lower frequencies. However, since the bending timescale T_o is on the order of a few months for many PCs,

it is generally poorly resolved in monthly data due to the sample errors occurring at the timescale near the sampling timescale (i.e., a month). When using daily PCs (obtained by projecting the daily data onto the EOF patterns of monthly data), the bending timescale T_o is much better resolved. The shapes of the spectra of daily PCs can be characterized by Eq. (8). The timescales at which the spectra become flat are comparable to the values of T_o shown in Fig. 1. (The spectra of the first two PCs are similar to those shown in Figs. 7a and 8a.)

The absolute low-frequency variance depends on the spectral level of the white noise and cannot be directly inferred from an analysis of T_o. However, an EOF analysis using data containing only variations on timescales of decades has shown that the reddest modes identified here remain the leading EOFs at frequencies lower than one cycle every few decades (von Storch 1994) and, therefore, represent motions with the largest absolute variance at these low frequencies.

The first two EOFs of the 200-hPa streamfunction are distinctly different from all other EOFs, not only in terms of their temporal characteristics as described by T_o, but also in terms of their spatial structures. Figure 2 shows the first four EOFs of the 200-hPa streamfunction. The reddest modes (Figs. 2a and 2b) are strongly anisotropic and clearly prefer the zonal direction, although they are not strictly zonally symmetric. In contrast, EOF3 and EOF4 (Figs. 2c and 2d) and all higher-order EOFs of the streamfunction reveal wavy structures. The EOFs of the velocity potential are even more isotropic (not shown). The first one of the 300-hPa velocity potential essentially describes global-scale wavenumber-1 divergence with one center being located in the equatorial Eastern and the other center with opposite sign in the equatorial Western Hemisphere. The related horizontal motions do not prefer any specific direction. It appears that the timescale T_o is correlated with the degree of isotropy of motions. The larger T_o is, the more anisotropic the motion is.

Some readers might expect that the teleconnection modes (Wallace and Gutzler 1981), such as that describing the North Atlantic oscillation (NAO), also vary on long timescales and must therefore have red spectra. The ECHAM1/LSG model does produce teleconnection modes. EOF3 in Fig. 2, for instance, bears some resemblance with the Pacific North American pattern. An EOF analysis showed that a mode similar to the NAO appears as the most dominant mode of the Northern Hemispheric geopotential height (von Storch et al. 1997). That the teleconnection modes do not show up as the reddest modes in the present analysis may be caused by the following two facts.

First, the teleconnection modes are usually described using hemispheric geopotential height, whereas the present study considers the global fields of the streamfunction and velocity potential. Since global-scale horizontal motions are completely described by the global fields of streamfunction and velocity potential, but not by hemispheric geopotential height alone, the teleconnection modes need not necessarily be the reddest modes of all motions. Second, the teleconnection modes are usually studied using winter data since they tend to have relatively large amplitudes during the wintertime. The result of this paper, however, is derived from year-round monthly data and can therefore not be directly compared to studies using winter data only.

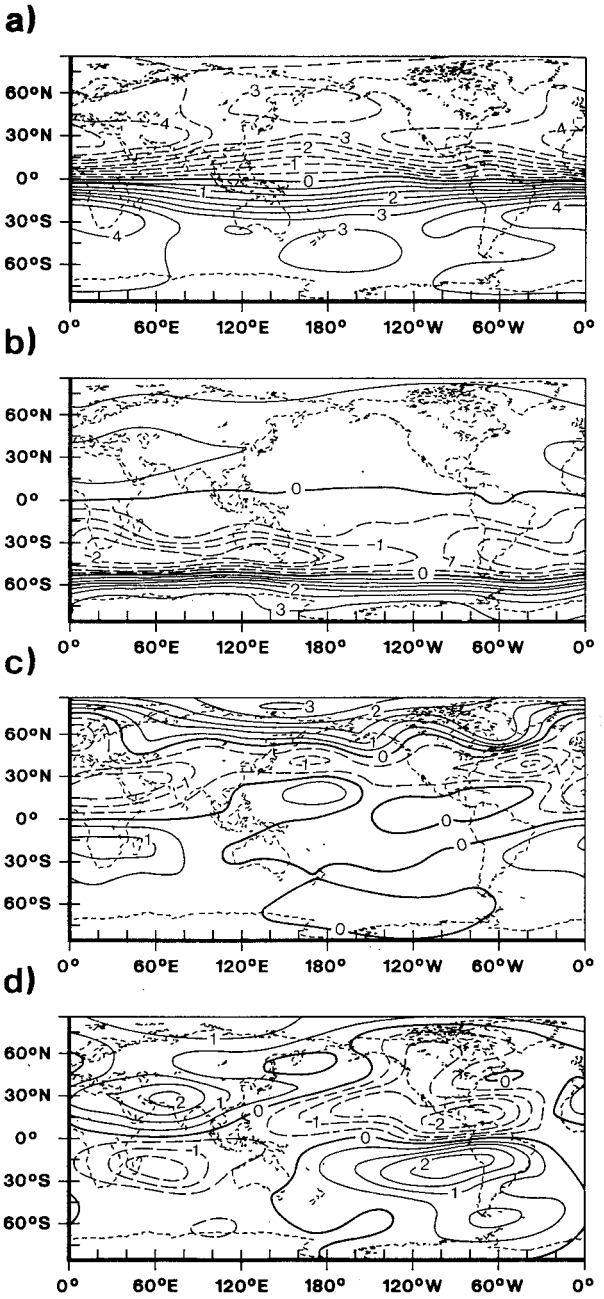

FIG. 2. The first four EOFs as derived from 500-yr monthly anomalies of the 200-hPa streamfunction. The anomalies are obtained by subtracting the 500-yr mean annual cycle.

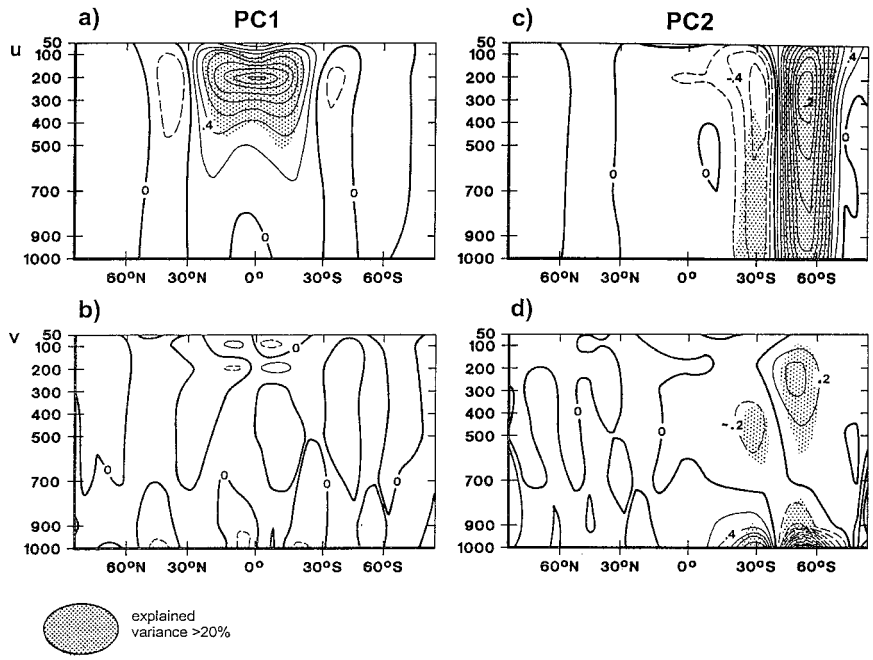

FIG. 3. Regression patterns between PCs and zonally averaged zonal velocity (upper) and meridional velocity (lower), with (a) and (b) on the left for PC1 and (c) and (d) on the right for PC2. The shaded areas indicate areas where the variance explained by the corresponding regression patterns is larger than 20% of the monthly unfiltered variance. Since PCs are normalized, the anomalies are in physical units with zonal wind in m s^{-1} and meridional wind in 10^{-1} m s^{-1}.

3. Spatial characteristics of the reddest modes

As already mentioned in section 2, the two reddest modes have different vertical structures. In order to obtain the global spatial characteristics of these modes, maps of regressions between the normalized monthly PC1/2 of the 200-hPa streamfunction and other atmospheric variables are calculated. The amplitudes of anomalies shown in a regression pattern represent one-standard-deviation anomalies. All regression patterns are calculated from 500-yr monthly anomalies. Because of the strong anisotropy found in the streamfunction (Figs. 2a and 2b), I will concentrate on the meridional and vertical distribution of these modes.

Figure 3 shows regression patterns between PCs and zonally averaged zonal and meridional wind. Consistent with the streamfunction shown in Figs. 2a and 2b, EOF1 is related to a maximum of the zonal wind anomalies centered at the equator in the upper troposphere (Fig. 3a) and EOF2 is related to a dipole structure of the zonal wind anomalies located at Southern Hemispheric mid- and high latitudes (Fig. 3c). The meridional extension of these anomalies covers 50°–60° of latitude. The amplitudes reach about 1–2 m s^{-1} for both modes. The significance of these wind patterns is suggested by the percentage of the explained variances. The shaded areas in Fig. 3 indicate regions where the variance explained by the regression pattern is larger than 20% of the total unfiltered monthly variance. They coincide with the regions of large wind anomalies and have maximum values of about 40%–70%. In the following, the mode described by PC1 of 200-hPa streamfunction is referred to as the tropical mode and that by PC2 as the Southern Hemisphere mode.

The vertical-meridional sections show the difference in the vertical structures of the two modes. The tropical mode is confined to the upper troposphere and almost disappears entirely below 700 hPa (Fig. 3a). In contrast, the zonal wind anomalies related to the Southern Hemisphere mode extend throughout the entire troposphere.

Consistent with the strong anisotropy already seen in Figs. 2a and 2b, the anomalies of meridional velocity (Figs. 3b and 3d) are found to be much smaller than those of zonal velocity. This is particularly true for the tropical mode (Fig. 3b). For the Southern Hemisphere mode (Fig. 3d) the anomalies of meridional velocity reach about 0.02–0.04 m s^{-1} in the troposphere, and about 0.3 m s^{-1} at the surface. The ratio of the meridional velocity to zonal velocity is on the order of 10^{-2} in the troposphere and on the order of 10^{-1} at the surface. Although the amplitudes are small, the corresponding pattern (Fig. 3d) is significant in terms of the explained variance. Maximal explained variance of about 60% is found near the surface at about 50°–60°S, and about 45% in the upper troposphere at about the same latitudes. It indicates a meridional circulation with an anomalous divergence at lower levels and an anomalous convergence at upper levels.

Regression patterns are also calculated for two ver-

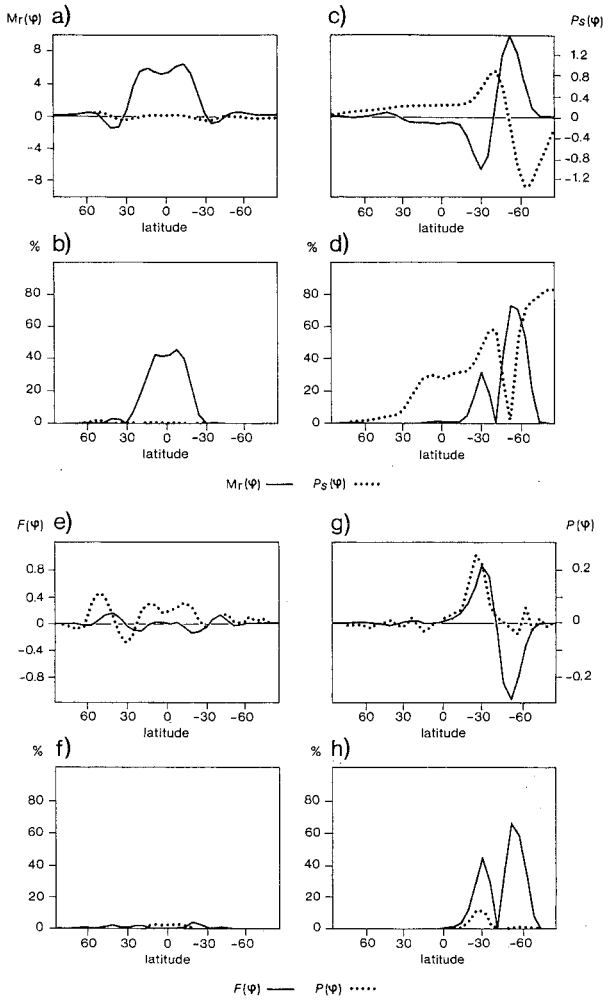

FIG. 4. Regression patterns between PCs and both vertically and zonally integrated relative angular momentum, $M_r(\varphi)$ [solid line in (a) and (c)], and zonally averaged area-weighted surface pressure, $p_s(\varphi)\cos\varphi$ [dotted line in (a) and (c)]. The curves on the left-hand side are related to PC1 and those on the right-hand side to PC2. (b), (d) The explained variances are shown below the regression patterns. The $M_r(\varphi)$ is given in 10^5 Hadley seconds, where 1 Hadley $= 10^{18}$ kg m^2 s^{-2}, and $p_s(\varphi)$ is in hPa.

tically integrated variables (Fig. 4). They are the zonally and vertically integrated relative angular momentum, $M_r(\varphi)$ (solid line in Figs. 4a and 4c), and the total mass in a vertical column, which is given by zonally averaged surface pressure $[p_s]$ weighted by cos φ (dotted line in Figs. 4a and 4c). The quantity $[p_s]$ cos φ is related to Ω angular momentum M_Ω according to Eq. (4). The term $M_r(\varphi)$ is calculated in such a way that $M_r = \Sigma_\varphi M_r(\varphi)$. The percentages of the variance explained by the meridional profiles of $M_r(\varphi)$ and $[p_s]$ cos φ are shown in Figs. 4b and 4d.

The tropical mode is related to anomalies of $M_r(\varphi)$ centered at the equator, and the Southern Hemisphere mode to a dipole structure of $M_r(\varphi)$ in the Southern Hemispheric mid- and high latitudes. In terms of both amplitude and explained variance, surface pressure anomalies are not related to the tropical mode (dotted line in Figs. 4a and 4b) but are significantly related to the Southern Hemisphere mode (dotted line in Figs. 4c and 4d).

TABLE 1. One-standard-deviation anomalies in relative (M_r) and Ω angular momentum (M_Ω) related to PC1 and PC2 of the 200-mb streamfunction. The term M_r is calculated from the zonal wind anomalies shown in Figs. 3a and 3c, whereas M_Ω is calculated from surface pressure anomalies shown in Figs. 4a and Fig. 4c (dotted lines). Both M_r and M_Ω are given in Hadley seconds, where 1 Hadley $= 10^{18}$ kg m^2 s^{-2}.

	PC1	PC2
M_r	4.7×10^6	6.1×10^5
M_Ω	1.8×10^4	1.7×10^6

In summary, the tropical and the Southern Hemisphere modes are modes with large meridional scale. Both reveal a strong anisotropy, with zonal velocity being much larger than meridional velocity. The difference between the two modes is related to the vertical structure of zonal velocity, the meridional circulation, and the mass redistribution. The tropical mode is located in the upper troposphere, whereas the Southern Hemisphere mode has large anomalies of zonal velocity throughout the entire troposphere. A meridional circulation and a mass redistribution are found to be related to the Southern Hemisphere mode, but not to the tropical one.

4. Relationship between the reddest modes and the global relative and Ω angular momenta

The different ways in which mass is involved, as shown in section 3, suggest that the tropical and the Southern Hemispheric modes contribute differently to the global Ω angular momentum, although both modes are related to a large amount of relative angular momentum. The situation is further quantified in Table 1, in which the relative and Ω angular momenta relative to each mode are listed. The values of the angular momenta are derived from the anomalies of zonal wind and surface pressure shown in the regression patterns. Because regression patterns reveal one-standard-deviation anomalies, the numbers in Table 1 represent one-standard-deviation anomalies of M_r and M_Ω related to PC1 and PC2. The most striking feature of Table 1 is that the tropical mode possesses essentially only relative angular momentum, with M_r being two orders of magnitude larger than M_Ω, whereas the Southern Hemisphere mode possesses both Ω angular momentum and relative angular momentum, but with M_Ω being about a factor 3 larger than M_r.

Table 1 also shows that when considering only motions related to the tropical and the Southern Hemisphere modes, the global relative angular momentum M_r is essentially controlled by the tropical mode (since M_r related to PC1 is about one order of magnitude larger

than that related to PC2), whereas the global Ω angular momentum M_Ω is essentially controlled by the Southern Hemisphere mode (since M_Ω related to PC2 is about two orders of magnitude larger than that related to PC1). What happens when other motions are also considered? Would the tropical and the Southern Hemisphere modes still make, respectively, the largest contributions to M_r and M_Ω and therefore control, respectively, the variations of M_r and M_Ω?

In order to answer these questions, coherence and phase spectra between M_r/M_Ω and PC1/2 of the 200-hPa streamfunction are calculated (Fig. 5). The spectra shown in Fig. 5 consist of two parts. The high-frequency part is derived from 10 yr of daily data (model years 91–100), and the low-frequency part from 500 yr of monthly data. Both the high- and low-frequency spectra are estimated from five consecutive segments. The method of deriving the whole spectrum from differently resolved data is chosen for practical reasons. It is a time-consuming job to extract the 500-yr three-dimensional daily fields that are required for the angular momentum calculation from the 1260-yr archive. The major outcome of this procedure is an extremely high resolution at the high-frequency end of the spectrum. Using a Fourier transform for a 100-yr daily time series, several thousands of frequencies are resolved between $\frac{1}{2}$ and $\frac{1}{3}$ cycles per day. Such a high resolution at high frequencies is not necessary for the current problem. The ability of the method, which uses daily and monthly data to describe the whole spectrum, is indicated by the comparable spectral levels of daily and monthly spectra at the overlapping frequencies. However, the comparison cannot be made in terms of each individual spectral peak. This is not only because of the random character of the time series, which prevents an interpretation of every peak, but also because of the different spectral resolutions of the data used and the sampling errors.

Figure 5 shows a highly coherent in-phase relationship between PC1 and M_r and between PC2 and M_Ω at frequencies of about one cycle per month down to the lowest resolvable frequency and no relationship at frequencies higher than one cycle per month. This suggests that on timescales of about a month up to several decades (which are well resolved in a 500-yr monthly time series), the tropical and Southern Hemisphere modes are the most intense motions relative to all other modes that contribute to variations of M_r and M_Ω, such that they control the variations of M_r and M_Ω, respectively. On timescales shorter than a month, the reddest modes become weaker than the other motions and lose their control over the variations of M_r and M_Ω.

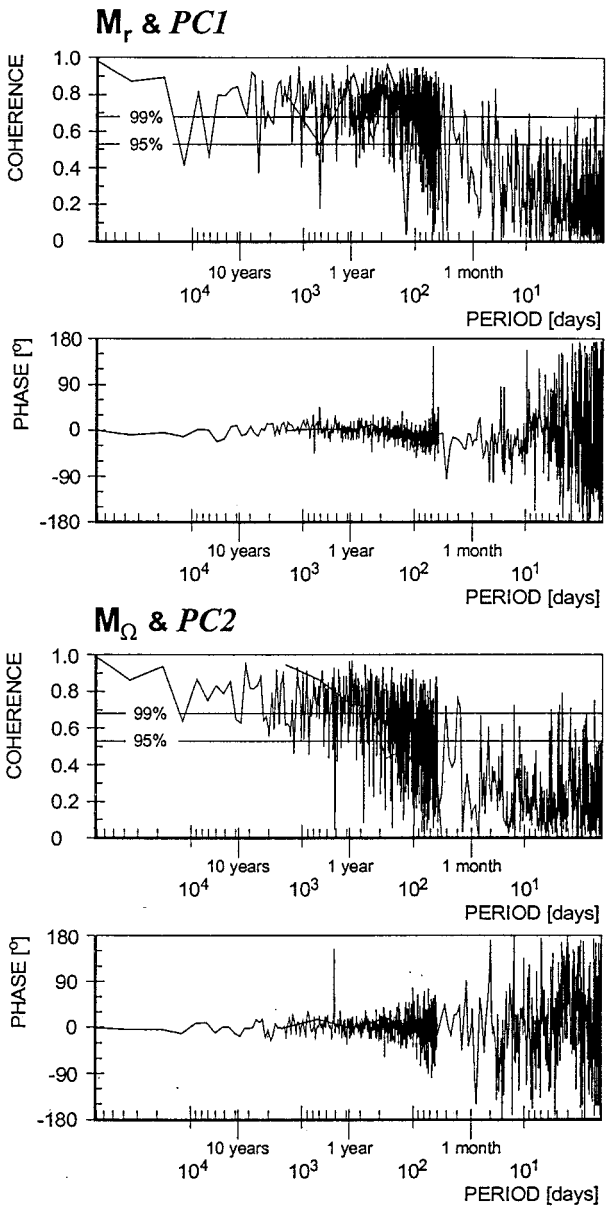

FIG. 5. Phase and coherence spectra between (a) PC1 and the relative angular momentum M_r and (b) PC2 and the Ω angular momentum M_Ω. Since PC1 and PC2 are derived from anomalies, the annual cycle is also removed from the time series of M_r and M_Ω. The two horizontal lines in the coherence spectra indicate the 99% and 95% confidence levels, respectively.

5. Forcings of the spectra of the reddest modes

The relationship shown in Fig. 5 suggests that the torques of M_r and M_Ω must be, respectively, the forcings of the variations of the tropical and Southern Hemisphere modes on timescales ranging from one month to the longest resolvable timescale. Following this suggestion, characteristics of the forcings of the reddest modes are studied by considering the budgets of M_r and M_Ω. To be sure that the ECHAM1/LSG model does a reasonable job in producing the angular momenta and their torques, the performance of the model in simulating the annual cycles of the angular momenta and the torques, for which observations are available, is first discussed.

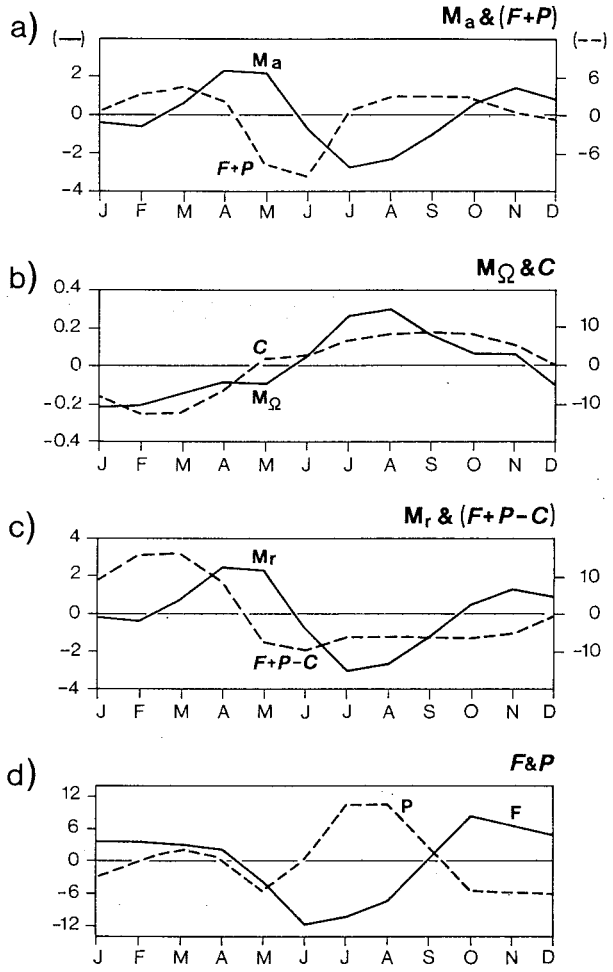

FIG. 6. (a)–(c) Annual cycles of the absolute, Ω, and relative angular momenta (M_a, M_Ω, M_r) and their corresponding forcings, and (d) the annual cycles of friction (solid line) and pressure (dashed line) torque. The 500-yr means are removed. Angular momentum terms are given in 10^7 Hadley seconds, and torques in Hadleys.

a. Annual cycles of angular momenta and their torques

Figures 6a–6c show annual cycles of the global absolute angular momentum M_a, the Ω angular momentum M_Ω, and the relative angular momentum M_r, and their corresponding torques. The contributions of the friction and pressure torques, $\mathcal{F}$ and $\mathcal{P}$, to the total torque, shown by the dashed line in Fig. 6a, are illustrated in Fig. 6d. The zero lines in Fig. 6 correspond to the 500-yr means.

The absolute angular momentum M_a shows a rapid decrease from May to July and a rather broad maximum in the northern winter and spring with a secondary minimum in late January and February (solid line in Fig. 6a). Apart from January and February, the annual cycle is consistent with the individual seasonal cycles, which have been presented by Rosen and Salstein (1983) and Rosen (1993). The presence of the secondary minimum in January and February makes the semiannual component in the model stronger than the annual component, whereas, in the observations, the first harmonic is clearly the dominant variation on seasonal timescales. The secondary minimum in late January and February is also found in other GCMs (Boer 1990; Rosen et al. 1994).

The amplitude of the annual cycle of the Ω angular momentum M_Ω (solid line in Fig. 6b) is about 10 times smaller than that of the relative angular momentum M_r (solid line in Fig. 6c). It is noted that the ratio of the anomalies of M_Ω to those of M_r on the annual timescale is smaller than that as derived from the reddest modes in Table 1, indicating that the variation of M_Ω is more important on nonseasonal than on seasonal timescales. The annual cycle of M_Ω is characterized by an increase from its minimum in February to its maximum in August, and a decrease thereafter. The annual cycle and the annual range of M_Ω are in good agreement with observations (R. D. Rosen and P. Nelson 1994, personal communication).

The annual cycles of $\mathcal{C}$ and $\mathcal{F} + \mathcal{P} - \mathcal{C}$ (dashed lines in Figs. 6b and 6c) cannot be compared with the observations, since the Coriolis conversion term $\mathcal{C}$ has not been considered using observational data. The annual cycle of the pressure torque (dashed line in Fig. 6d) is in qualitative agreement with that shown by Wahr and Oort (1984), especially with the pressure torque cycle that they obtained using the ''z method.'' The minimum in early northern summer and the maximum in northern autumn appear about one month later than in the observations. The friction torque (solid line in Fig. 6d) cannot be directly compared with observations due to problems in obtaining accurate surface stresses. Different annual cycles of friction torque were found in other, different GCMs (Wahr and Oort 1984; Boer 1990). The performance of the ECHAM1/LSG model in simulating the annual march of the global angular momenta and their torques is, in a broad sense, reasonable.

b. Forcings of the spectra of the reddest modes

In this section, the forcings of the tropical and Southern Hemisphere modes are studied by considering the budgets of M_r and M_Ω, which are described in terms of the spectra shown in Figs. 7 and 8. The study is confined to the low-frequency range, over which a connection between the reddest modes and M_r and M_Ω has been found (Fig. 5).

The upper two diagrams of Figs. 7 and 8 show the power spectra of M_r, M_Ω, and their corresponding torques. The spectra of M_r and M_Ω have shapes similar to those of the time series of the tropical and Southern Hemisphere modes (not shown). Spectral peaks are found at the seasonal timescales (e.g., 1 yr and 0.5 yr) and at the longest resolved timescale. The spectral peak at the latter is induced by the fact that the time-mean torques in the model, defined as the 500-yr averages, are not zero, so that M_r and M_Ω are characterized by long-term trends. Apart from these peaks, the spectra

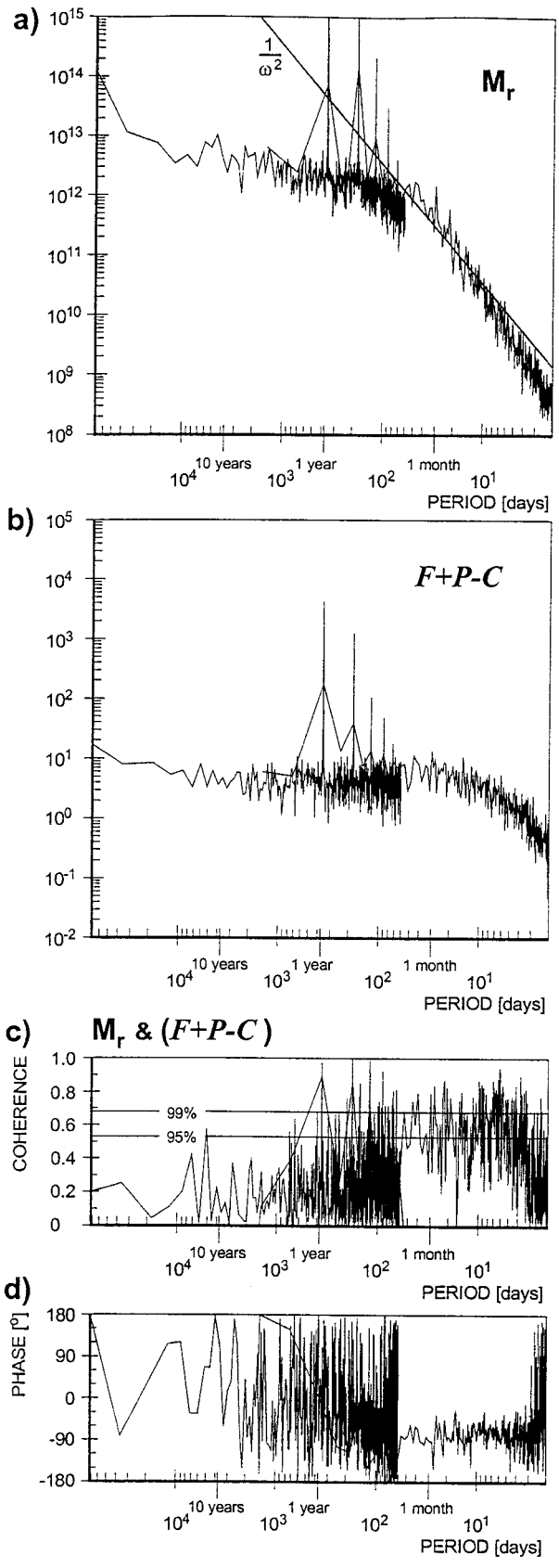

of M_r and M_Ω are essentially red. The low-frequency parts of the spectra are flat, whereas the high-frequency parts are proportional to ω^{-2}. The bending timescales for both M_r and M_Ω are somewhere between about a half of a year and a year. The torques of M_r and M_Ω (Figs. 7b and 8b) are essentially flat.

The lower two diagrams of Figs. 7 and 8 show the coherence and phase spectra between M_r and M_Ω and their corresponding torques, that is, $\mathcal{F} + \mathcal{P} - \mathcal{C}$ and $\mathcal{C}$, with $\mathcal{C}$, $\mathcal{F}$, and $\mathcal{P}$ as defined in Eqs. (5)–(7). In both cases, one does not find the perfect 90° out-of-phase relationship that is expected from the angular momentum equations. At timescales shorter than a year, there are some coherences between M_r and its torque and M_Ω and its torque. But the correlations are far from perfect. At timescales longer than a year, M_r and M_Ω are not correlated with their torques. The phases are irregular and the coherences are insignificant.

Certainly, the problems in closing the global angular momentum budgets may be caused by errors made in calculating M_r, M_Ω, $\mathcal{F}$, $\mathcal{P}$, and $\mathcal{C}$ according to Eqs. (3)–(7). In these calculations, several assumptions, such as the hydrostatic approximation, the smallness of vertical velocity relative to meridional velocity, and a dry atmosphere, are used. Apart from these, the metamorphosis of the original differential equations of motion to the discrete difference equations laden with many parameterized processes (such as gravity wave drag, which has not been included in $\mathcal{F}$ but is present in the model) might also cause errors. Furthermore, errors might have been introduced when I calculated the global integrals not from the model hybrid vertical coordinate, but from the usual pressure levels after some vertical interpolations. Another error results from the specific format of the model output. The output is on a twice-daily basis. However, the output of surface stress is in 12-h averages, whereas that of surface pressure is an instantaneous value every 12 h. Consequently, the friction and mountain torques cannot be calculated in a consistent manner. Finally, there are also the sampling errors that occur when monthly averaged or daily sampled time series are used instead of time series that are generated at each integration time step (40 min) of the model. The values at each integration time step are, however, not stored in the output. Due to the model-specific nature of some of the errors, it is impossible to obtain error-free estimates of M_r, M_Ω, $\mathcal{F}$, $\mathcal{P}$, and $\mathcal{C}$ from this particular model output.

However, we are not interested in the question of how to make error-free estimates of the angular momenta

←

FIG. 7. Autospectra of (a) the global relative angular momentum M_r, and (b) its torque ($\mathcal{F} + \mathcal{P} - \mathcal{C}$), and the (c) coherence and (d) phase spectra between them. The two horizontal lines in the coherence spectrum indicate the 99% and 95% confidence levels, respectively. Straight line in (a) indicates the $1/\omega^2$ slope.

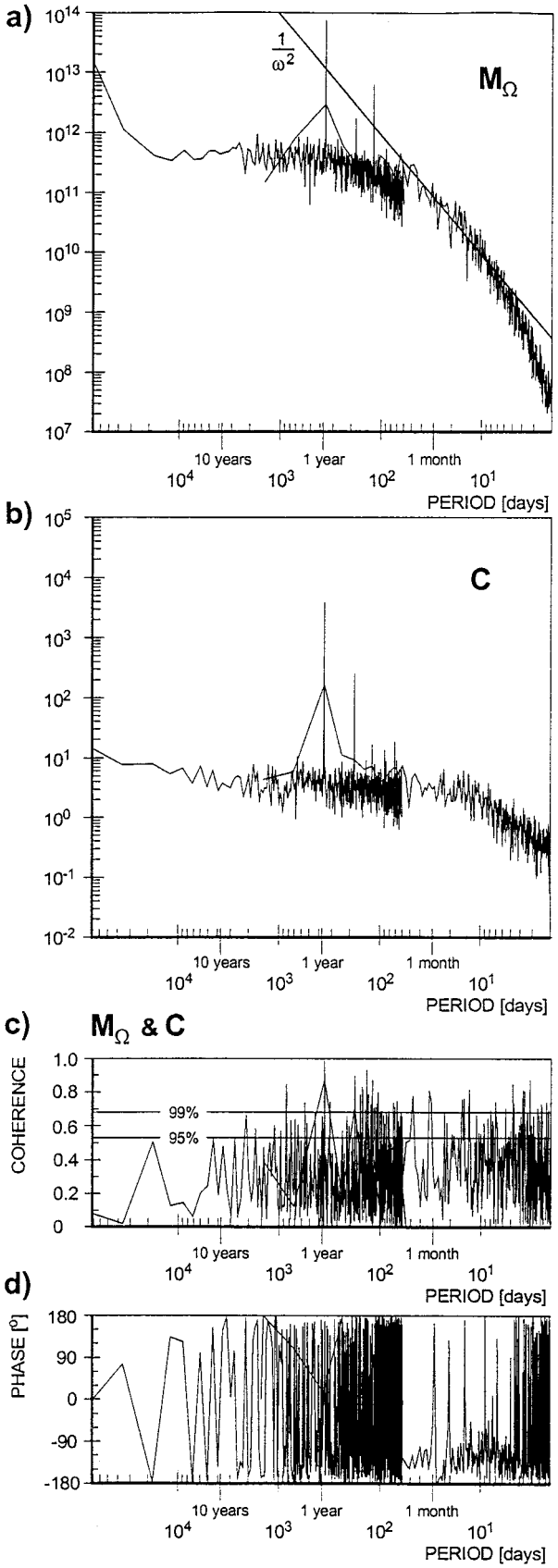

and their torques, but in the characteristics of the spectral forcings of the reddest modes. In the following, two suggestions as to these characteristics are made, despite the estimation errors.

The first one concerns the forcings of *high-frequency* variations of M_r and M_Ω and therefore also those of the *high-frequency* part of the spectra of the reddest modes. Hereafter, ''high frequency'' refers to frequencies of about one cycle per every few months down to one cycle per year. The cause for nonperfect coherences at these high frequencies can be seen by comparing Figs. 7c and 7d and 8c and 8d with Fig. 9, which shows the coherence and phase spectra between the global absolute angular momentum M_a and its torque, $\mathcal{F} + \mathcal{P}$. The comparison shows that, at high frequencies, the coherence between M_r/M_Ω and the corresponding torque, which involves the Coriolis conversion term $\mathcal{C}$, is much less significant than the coherence between the global absolute angular momentum M_a and its torque, which does not involve $\mathcal{C}$. A similar situation is obtained for the annual variations shown in Fig. 6. While $\mathcal{F} + \mathcal{P}$ is 90° out of phase with M_a (Fig. 6a), $\mathcal{C}$ is essentially in phase with M_Ω (Fig. 6b) and M_r increases from July to November despite the negative values of $\mathcal{F} + \mathcal{P} - \mathcal{C}$ (Fig. 6c). On both seasonal and nonseasonal timescales, the largest problem is found for M_Ω, whose forcing is entirely controlled by the Coriolis conversion term $\mathcal{C}$. These results strongly suggest that $\mathcal{C}$ is much more poorly estimated than $\mathcal{F}$ and $\mathcal{P}$.

The Coriolis conversion term $\mathcal{C}$ is estimated from the meridional velocity at nine levels, with the two lowest levels being 1000 and 900 hPa. Figure 3d shows, however, that meridional velocity is strongly nonuniform in the vertical direction, with large values being confined to a thin layer near the surface. The poor quality of the estimation of $\mathcal{C}$ may therefore be caused by the too-coarse vertical resolution near the surface used for the global integration in Eq. (5). This indicates that the true Coriolis conversion term, which is responsible for the variations of M_Ω and therefore also for those of the Southern Hemisphere mode, involves processes that produce large meridional velocity at the surface.

The second suggestion concerns the forcings of *low-frequency* variations of M_r and M_Ω, and therefore those of the *low-frequency* part of the spectra of the reddest modes. Hereafter, ''low frequency'' refers to frequencies of about one cycle per year to one cycle per several decades. At these low frequencies, variations of M_r and M_Ω are not related to those of their torques. Even for the variations of M_a, whose torque does not involve the

←

FIG. 8. Autospectra of (a) the global Ω angular momentum M_Ω, and (b) the Coriolis conversion term $\mathcal{C}$, and the (c) coherence and (d) phase spectra between them. The two horizontal lines in the coherence spectrum indicate the 99% and 95% confidence levels, respectively. Straight line in (a) indicates the $1/\omega^2$ slope.

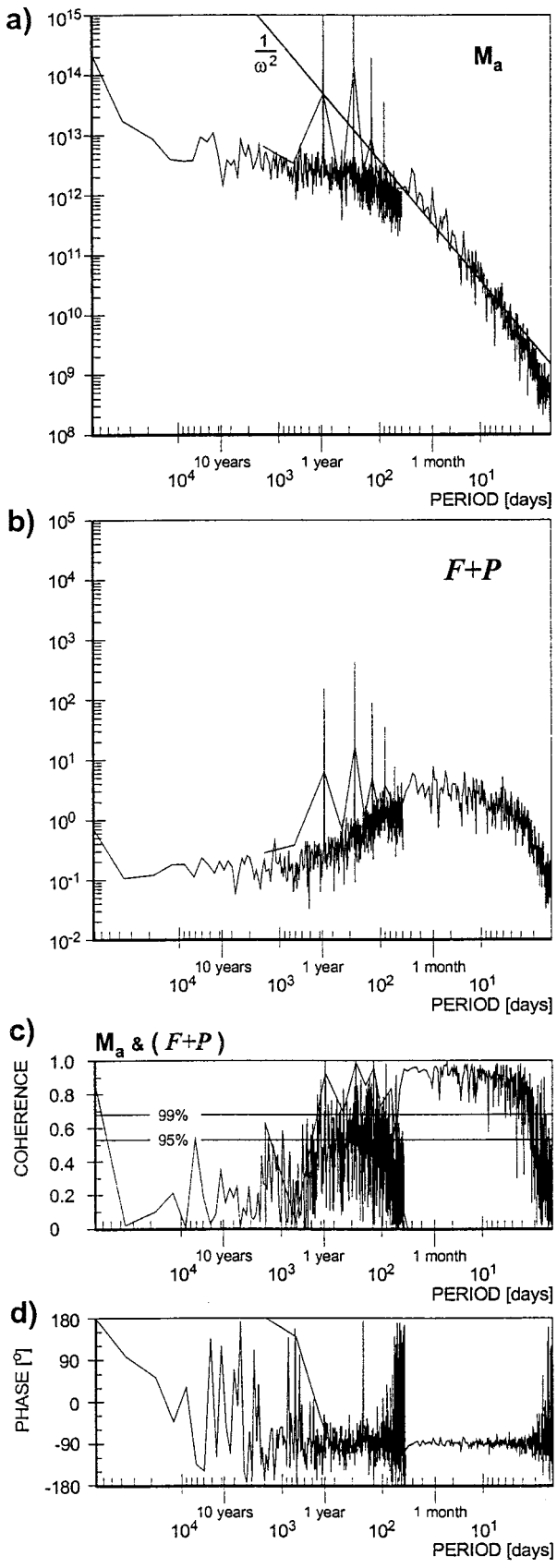

Coriolis conversion term (which is difficult to estimate), the coherence at low frequencies is insignificant. It appears that, relative to the spectral level of the true torques, the estimation errors increase with decreasing frequency or, equivalently, that, for a given level of estimation error noise, the spectra of the true torques decrease with decreasing frequency.

Can the spectra of the true torques decrease with decreasing frequency? An inspection of the angular momentum equation suggests that this can indeed happen. Following the angular momentum constraint, the spectrum of the angular momentum equals the spectrum of the corresponding torque multiplied by ω^2. If the spectrum of the angular momentum is flat at low frequencies, the spectrum of the corresponding torque would decrease with decreasing frequency at the rate ω^2. Consideration of Figs. 7a and 8a suggests that when the spectral peaks at the lowest resolved frequency (which are induced by the nonzero time-mean torques in the model) are ignored and only fluctuations are concentrated on, the spectra of angular momenta M_r, M_Ω, and M_a are flat at low frequencies. Under these circumstances, the spectra of the true torques must decrease with decreasing frequency. The true forcings for the low-frequency angular momentum variations and likely also those for the low-frequency variations of the reddest modes can then be easily swamped by estimation errors, so that it is extremely difficult to identify these forcings.

6. Summary

This paper is concerned with the reddest atmospheric modes (i.e., modes having the reddest spectra) and the forcings of the spectra of these modes in a multicentury integration with the coupled ECHAM1/LSG model.

By fitting an AR(1) process to the considered time series, the spectrum is characterized by the parameter of the fitted AR(1) process. In particular, the bending timescale T_o, which is a function of the parameter of the fitted AR(1) process, can be used as a simple measure of the redness. Consideration of T_o allows an objective intercomparison of spectral shapes.

Using the estimated values of T_o, the first two PCs of the 200-hPa streamfunction are identified as the time series that have the reddest spectra in the ECHAM1/LSG integration. They describe motions centered at the equator and located at the Southern Hemispheric mid- and high latitudes and are referred to as the tropical and the Southern Hemisphere modes, respectively. The essentially zonally oriented anomalies of the streamfunction and the small ratio of meridional velocity to zonal

←

FIG. 9. Coherence spectrum and phase spectrum between the global absolute angular momentum M_a and its torque. The two horizontal lines in the coherence spectrum indicate the 99% and 95% confidence levels, respectively.

velocity indicate that the two modes are anisotropic. The meridional scale of the two modes extends over about 50°–60° of latitude and is therefore comparable to the radius of the earth.

The detailed structures of the two reddest modes are distinctly different from each other. The tropical mode describes zonal wind variations in the upper troposphere and is not significantly related to anomalies of surface pressure and meridional velocity. The Southern Hemisphere mode, on the other hand, reveals a dipole structure of zonal wind in the entire troposphere and is accompanied by a well-defined meridional circulation and a well-defined mass redistribution.

Due to different ways in which mass and zonal wind are involved, the two reddest modes contribute differently to the global relative and Ω angular momentum. The tropical mode has a larger relative angular momentum M_r than Ω angular momentum M_Ω, whereas the reverse is true for the Southern Hemisphere mode. Moreover, on timescales longer than a month or so, the tropical mode controls the variations of M_r and the Southern Hemisphere mode controls the variations of M_Ω. The result suggests that relative to all motions that contribute to variations of M_r and M_Ω, the two modes are the most intense low-frequency motions in the ECHAM1/LSG integration.

Based on the relationships between the reddest modes and the global angular momenta, the separate budgets of M_r and M_Ω were used to study the forcings of the spectra of the reddest modes. The results indicate that the true forcings of the low-frequency parts of the spectra are extremely feeble and cannot be easily identified. The true forcings of the high-frequency parts of the spectra, however, can be captured, in particular when reducing the errors made in estimating the Coriolis conversion term $\mathcal{C}$. The analysis suggests that the large estimation errors in $\mathcal{C}$ are caused by using too-coarse vertical resolution near the surface for the evaluation of the global integral. It is suggested that the true forcing of the high-frequency variations of M_Ω, and therefore also that of the high-frequency variations of the Southern Hemisphere mode, is affected by processes that involve large meridional velocity near the surface.

Structures that resemble the reddest modes discussed in this paper have also been found in both observations and GCM simulations, though the redness, or in general the spectral features, of these modes has not been studied. Rogers and van Loon (1982) performed an EOF analysis for 8 yr of Southern Hemisphere data from the Australian Bureau of Meteorology. The leading EOF patterns in sea level pressure and 500-hPa geopotential heights are similar to each other. Heights or pressures poleward of 50°S rise and fall in opposition to those at lower latitudes. This meridional mass distribution is comparable to that shown by the dashed line in Fig. 4c. Such mass variations have also been documented by Trenberth and Christy (1985). In an attempt to capture the linearly behaving modes in the observed atmosphere–ocean system (Xu 1993), the changes in the Southern Hemispheric circulation that might be related to such mass variations were identified. Recently, Kang and Lau (1994) found that the global relative angular momentum is highly correlated with the first EOF of the upper-level streamfunction using the analysis of the European Centre for Medium-Range Weather Forecasts. This eigenvector is similar to EOF1 in Fig. 2a. Since the tropical mode is not related to mass anomalies, one fails to identify this mode by using pressure or geopotential heights. This might be the reason why this mode had not been described earlier.

A similar situation is found when analyzing GCM outputs. A mode comparable to EOF2 has been produced by both the T20 Canadian Climate Centre model (Zwiers 1987) and the R15 Geophysical Fluid Dynamics Laboratory model (Lau 1981). The tropical mode could not be identified, since in both studies only pressure and geopotential heights were considered. In a 6000-day perpetual-January integration performed by the National Center for Atmospheric Research Community Climate Model, Branstator (1990) found a mode that is similar to EOF1 in Fig. 2a by considering the streamfunction.

Acknowledgments. I express my gratitude to Hans von Storch, Klaus Hasselmann, Peter Müller, Richard Rosen, Grant Branstator, and Reiner Schnur for many fruitful discussions. Thanks also to Marion Grunert and Doris Lewandowsky for preparing the diagrams. The present analysis was done in the framework of the project ''Simulationen mit Klimamodelle über Hundert von Jahren: Analyse der interdekadischen Vairabilität und ihre Implikationen für die Signalerkenung von Climate Change,'' funded by the German Ministry for Education and Research.

REFERENCES

Boer, G. J., 1990: Earth–atmosphere exchange of angular momentum simulated in a general circulation model and implications for the length of day. *J. Geophys. Res.*, **95,** 5511–5531.

Branstator, G., 1990: Low-frequency patterns induced by stationary waves. *J. Atmos. Sci.*, **47,** 629–648.

James, I. N., and P. M. James, 1989: Ultra-low-frequency variability in a simple atmospheric circulation model. *Nature*, **342,** 53–55.

——, and ——, 1992: Spatial structure of ultra-low-frequency variability of the flow in a simple atmospheric circulation model. *Quart. J. Roy. Meteor. Soc.*, **118,** 1211–1233.

Lau, N.-C., 1981: A diagnostic study of recurrent meteorological anomalies appearing in a 15-year simulation with a GFDL general circulation model. *Mon. Wea. Rev.*, **109,** 2287–2311.

Kang, I.-K., and K.-M. Lau, 1994: Principal modes of atmospheric circulation anomalies associated with global angular momentum fluctuations. *J. Atmos. Sci.*, **51,** 1194–1205.

Peixoto, J.-P., and A. H. Oort, 1992: *Physics of Climate.* American Institute of Physics, 520 pp.

Robinson, W. A., 1991: The dynamics of the zonal index in a simple model of the atmosphere. *Tellus*, **43A,** 295–305.

——, 1993: The generation of ultralow-frequency variations in a simple global model. *J. Atmos. Sci.*, **50,** 137–143.

Rogers, J. C., and H. van Loon, 1982: Spatial variability of sea level

pressure and 500-mb height anomalies over the Southern Hemisphere. *Mon. Wea. Rev.,* **110,** 1375–1392.

Rosen, R. D., 1993: The axial momentum balance of the earth and its fluid envelope. *Surv. Geophys.,* **14,** 1–29.

——, and D. A. Salstein, 1983: Variations in atmospheric angular momentum on global and regional scales and the length of day. *J. Geophys. Res.,* **88,** 5451–5470.

——, ——, and S. L. Marcus, 1994: Model intercomparison of low-frequency signals in atmospheric angular momentum. *Proc. Sixth Conf. on Climate Variations,* Nashville, TN, Amer. Meteor. Soc., 1–4.

Trenberth, K. E., and J. R. Christy, 1985: Global fluctuations in the distribution of atmospheric mass. *J. Geophys. Res.,* **90** (D5), 8042–8052.

von Storch, J.-S., 1994: Interdecadal variability in a global coupled model. *Tellus,* **46A,** 419–432.

——, V. Kharin, U. Cubasch, G. C. Hegerl, D. Schriever, H. von Storch, and E. Zorita, 1997: A description of a 1260-year control integration with the coupled ECHAM1/LSG general circulation model. *J. Climate,* **10,** 1525–1543.

Wahr, J. M., and A. H. Oort, 1984: Friction- and mountain-torque estimates from global atmospheric data. *J. Atmos. Sci.,* **41,** 190–204.

Wallace, J. M., and D. G. Gutzler, 1981: Teleconnections in the geopotential height field during the Northern Hemisphere winter. *Mon. Wea. Rev.,* **109,** 784–812.

Xu, J.-S., 1993: The joint modes of the coupled atmosphere–ocean system observed from 1967 to 1986. *J. Climate,* **6,** 816–838.

Yu, J.-Y., and D. L. Hartmann, 1993: Zonal flow vacillation and eddy forcing in a simple GCM of the atmosphere. *J. Atmos. Sci.,* **50,** 3244–3259.

Zwiers, F. W., 1987: A potential predictability study conducted with an atmospheric general circulation model. *Mon. Wea. Rev.,* **115,** 2957–2974.